Steady-State Relative Permeability and Residual Trapping of $scCO_2$-Brine and N_2-Brine in Berea Sandstone: A Comparative Experimental Study

Naser Ansaribaranghar[1], *Maziyar* Mahmoodi[1], *Yueping* Yu[1], *Hamidreza* Shahosseini[1], *Mahsan* Basafa[1], *Alejandro* Romero Fragoso[1], *Lucky* Abiashue[1], *Lisa* Lun[2], *Daulet* Magzymov[3], *John* Molinaris[2], *and Lesley A.* James[1,*]

[1]Department of Process Engineering, Faculty of Engineering and Applied Science, Memorial University, St. John's, NL, A1B 3X5, Canada
[2]ExxonMobil Technology and Engineering Company, Spring, TX, USA
[3]ExxonMobil Upstream Integrated Solutions Company, Spring, TX, USA

Abstract. Accurate prediction of multiphase flow in CO_2 storage and related subsurface processes requires reliable relative permeability characterization. Supercritical carbon dioxide ($scCO_2$)-brine relative permeability experiments are technically demanding, such that N_2-brine relative permeability data are often used as surrogates. However, the validity of this substitution depends on rock type, flow regime, and test conditions. While controlled back-to-back coreflood studies show that replacing N_2 with $scCO_2$ can shift saturation endpoints and curve shapes in heterogeneous rocks under capillary limits, recent work on Berea sandstone reports that $scCO_2$-brine relative permeability is very similar to N_2-brine when tested on the same core at the same reservoir conditions, with both fluids exhibiting strongly water-wet behavior. These combined findings suggest that "N_2 as a surrogate" can be reasonable for Berea-type clean sandstones, but the validity must be verified under rigorous, steady-state experimental designs. Here, we use Berea sandstone as a benchmark to (i) provide an independent comparison of N_2-brine and $scCO_2$-brine k_r under identical steady-state conditions and (ii) extend the comparison to full saturation cycling including secondary drainage, which is directly relevant to reinjection and is rarely reported in the literature. Crucially, our baseline measurements are extensively cross-validated against foundational literature, showing good agreement with classical strongly water-wet relative permeability endpoints for analog fluid pairs. Furthermore, we analyze the residual capillary trapping characteristics of both fluid systems during the imbibition cycles. The trapping efficiencies and Land trapping coefficients derived from our experimental data are consistent with established empirical hysteresis models and historical benchmarks for homogeneous sandstones. By providing this rigorous, literature-validated dataset across full saturation paths, this work supports the use of N_2 as a non-wetting analogue for clean, strongly water-wet sandstones measured in the viscous-limit steady-state regime, and the use of standard Land and Corey parameterisations for such rocks. Extrapolation to heterogeneous or reactive formations should be made with caution and is identified as future work.

1 Introduction

Geological storage of carbon dioxide (CO_2) in deep saline aquifers is among the most promising routes to large-scale reduction of anthropogenic greenhouse-gas emissions [1,2]. Reliable simulation of plume migration, injectivity, and long-term security depends on relative permeability and capillary pressure functions measured at reservoir conditions [3-5]. The drainage and imbibition curves of the $scCO_2$-brine system govern plume distribution, while relative permeability hysteresis controls residual capillary trapping [6,7]. Residual trapping depends strongly on the maximum gas saturation reached at the end of drainage and is commonly parameterised with the empirical Land model [8]. Because real operations involve fluctuating injection, well shut-ins, and CO_2 reinjection [9,10], the secondary-drainage relative permeability is also important, yet is rarely reported [11,12].

Laboratory measurement of $scCO_2$-brine relative permeability at reservoir pressure and temperature is technically demanding [13,14], so nitrogen (N_2) is often used as a low-risk surrogate non-wetting phase, on the grounds that its interfacial tension and density contrast with brine reproduce comparable flow behaviour in many rocks [15,16]. This is reinforced by capillary-pressure testing showing that pristine, quartz-rich sandstones such as Berea remain strongly water-wet in the presence of $scCO_2$ [17,18], making the classically water-wet N_2-brine system an appropriate baseline analogue. Apparent differences reported in some corefloods are not thermodynamic in origin. Reynolds and Krevor [16] showed that, under capillary-limited conditions, the low

* Corresponding author: ljames@mun.ca

viscosity of $scCO_2$ (≈0.07 cP at the present conditions; [19]) makes the fluid sensitive to capillary heterogeneity and yields flow-rate-dependent 'effective' curves, whereas in the viscous limit the intrinsic $scCO_2$-brine relative permeability is invariant with conditions and consistent with N_2-brine. High-rate, steady-state recirculation studies confirm this agreement [16,20-23]. Systematic datasets spanning full saturation paths (drainage, imbibition, and secondary drainage) under a single steady-state protocol nevertheless remain scarce [19,24].

Most prior work has focused on clean quartzose sandstones such as Berea and Boise, where hysteresis, capillary-heterogeneity effects, and sensitivity to confining stress and brine salinity are well documented [2,21,25-27]. In reactive rocks, by contrast, dissolved CO_2 forms carbonic acid that drives coupled thermo-hydro-mechanical-chemical alterations (carbonate dissolution and wormholing, secondary mineral precipitation, clay swelling, and fines migration) that continuously change permeability, structural integrity, and trapping capacity [28-37]. Because these geochemical effects obscure the intrinsic, fluid-specific flow behaviour, isolating the latter requires a chemically inert, homogeneous benchmark, for which Berea sandstone is well suited. Most such studies have also relied on unsteady-state or centrifuge methods, which can introduce capillary-end-effect and viscous-fingering artefacts [38-41].

The present study addresses these gaps with a steady-state relative permeability campaign on a homogeneous Berea sandstone at identical reservoir conditions (30 MPa, 77 °C), applying the same fractional-flow schedule and apparatus to both $scCO_2$-brine and N_2-brine. The objectives are (i) to provide an independent, artifact-free comparison of N_2-brine and $scCO_2$-brine relative permeability under identical steady-state conditions; (ii) to extend the comparison across full saturation cycling (primary drainage → imbibition → secondary drainage), simulating reinjection; and (iii) to validate the measured endpoints, trapping efficiencies, and Land coefficients against foundational literature for clean quartzose sandstones.

The remainder of the paper is organised as follows. Section 2 describes the apparatus, core properties, fluid preparation, and steady-state methodology; Section 3 presents the measured relative permeability curves, endpoint saturations, and trapping characteristics; Section 4 discusses these results, benchmarking them against established empirical models and the wider literature and assessing the suitability of N_2 as a surrogate; and Section 5 summarises the key findings.

2 Materials and methods

2.1 Theoretical framework of steady-state multiphase flow

The simultaneous flow of $scCO_2$ (or N_2) and brine is described by the multiphase extension of Darcy's law. For horizontal, one-dimensional flow the volumetric rate of phase i is

$$q_i = \frac{k \cdot k_{r,i} \cdot A}{\mu_i} \cdot \frac{\Delta P_i}{L} \tag{1}$$

where k is the absolute permeability, $k_{r,i}$ the relative permeability of phase i, A the cross-sectional area, L the core length, μ_i the phase viscosity, and $\Delta P_i = P_{inlet} - P_{outlet}$ the (positive) pressure drop across phase i; with this convention the leading sign is positive.

In a steady-state coreflood the two phases are co-injected at a fixed fractional flow until the saturation profile is uniform; the capillary-pressure gradient then vanishes and the phase pressure drops are equal ($\Delta P_{nw} = \Delta P_w = \Delta P$), so the intrinsic relative permeability of each phase follows directly from the measured global pressure drop [16,25].

Hysteretic capillary trapping during imbibition is quantified with the empirical Land model [8], which relates the maximum initial gas saturation at the end of drainage (S_{gi}) to the residual gas saturation at the end of imbibition (S_{gr}):

$$S_{gr} = \frac{S_{gi}}{1 + C \cdot S_{gi}} \tag{2}$$

where C is the rock-specific Land trapping coefficient.

2.2 Apparatus and materials

All relative permeability measurements were performed using a high-pressure, high-temperature (HPHT) steady-state core-flooding apparatus designed for supercritical and gaseous non-wetting phases. A schematic diagram of the experimental setup is shown in **Fig. 1**. The system consists of a hydrostatic core holder [HYC-series, Vinci Technologies] rated to 40 MPa confining pressure and 100 °C, a Quizix® C-5000 Series dual-piston pump for precise brine injection, a Quizix® C-6000 Series dual-piston pump for $scCO_2$ injection, a Quizix® QX-20000 Series pump for overburden pressure control with silicone oil, Equilibar back-pressure regulators, Paroscientific Digiquartz® Series 6000 intelligent pressure transmitters (±0.01 % full-scale accuracy), and a high-pressure two-phase separator (New England Research, Inc.) equipped with an Acoustic Level Detection Module (ALDM) and ultrasonic transducers for real-time phase-volume and saturation monitoring. The entire recirculating flow loop was housed inside a Despatch RAF Series forced-convection oven maintained at a uniform 77 °C. Confining pressure was applied with silicone oil and maintained at 35 MPa (5 MPa above the 30 MPa pore pressure, equivalent to ~4350 psi) to simulate reservoir overburden conditions.

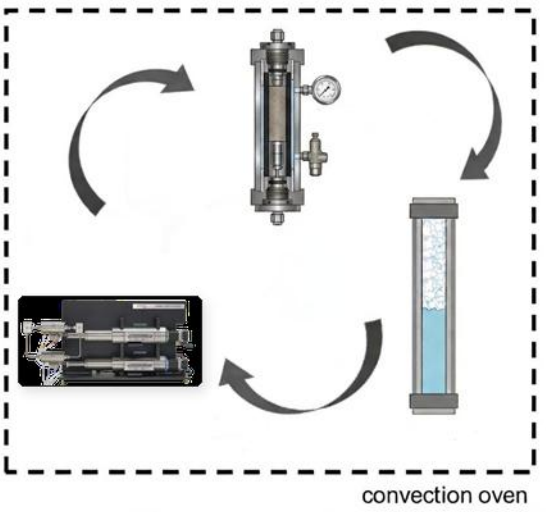

Fig. 1. Schematic diagram of the high-pressure/high-temperature recirculating steady-state coreflooding system. The apparatus includes dual Quizix pumps for precise fractional-flow control, a two-phase acoustic separator, absolute pressure transducers, and a temperature-controlled oven housing the entire flow loop.

Wetted metallic parts were Hastelloy alloys and all elastomeric seals were AFLAS (tetrafluoroethylene-propylene rubber) or FFKM to ensure chemical compatibility with scCO_2 and carbonic acid under HPHT conditions. Prior to each test the entire closed-loop system was cleaned by circulating toluene (to remove organic contaminants) followed by methanol (to remove salts and residual moisture), then purged with N_2. Full system integrity was verified through stepwise leak-hold testing (first with N_2, then with DI water/silicone oil) under target HPHT conditions using both static (pressure stability) and dynamic (pump displacement) methods. Upstream and downstream dead volumes were geometrically calibrated and incorporated into all material-balance calculations.

A single cylindrical Berea plug (diameter 3.82 cm, length 29.2 cm, porosity 18.8 % / 0.188 v/v) was used for all three corefloods; the test programme and the per-test absolute permeabilities are summarised in Table 1. XRD analysis of representative sample BR4 (**Fig. 2**) shows a quartz-dominated mineralogy, 87.3 wt% quartz with 3.4 wt% kaolinite and 5.1 wt% muscovite by whole-pattern fitting. We note that this bulk weight fraction is not a measure of the clay surface area that lines the pores, which can be disproportionately larger and is what governs reactivity; the high-salinity brine and fluid pre-equilibration described below were therefore important to suppress clay swelling and dissolution/precipitation. Prior to testing the core was cleaned with methanol and toluene, dried under vacuum, and vacuum-saturated with synthetic brine (4 wt% NaCl); the high-salinity brine inhibited swelling of the trace clays, preserving the native pore structure.

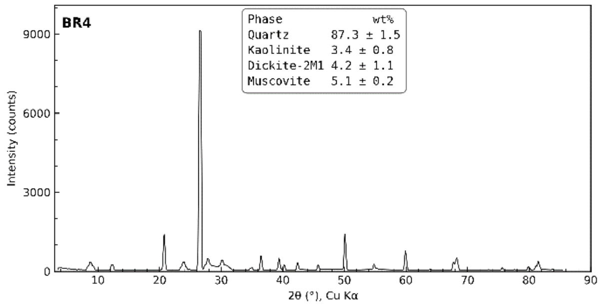

Fig. 2. X-ray diffraction (XRD) characterization of sample BR4: (a) measured diffractogram with identified mineral phases; (b) whole-pattern fitting (WPF/Rietveld-based) quantitative phase analysis indicating quartz as the dominant phase, with minor kaolinite, dickite, and muscovite.

Once fully saturated and stabilised under the 35 MPa net confining stress, the absolute brine permeability was 63.1 mD for the N_2 test and 61.8 mD for scCO_2 test #1 (clean plug), and 31.6 mD for scCO_2 test #2 (Table 1).

Establishing this absolute permeability under representative overburden stress is critical, as it serves as the baseline denominator for all subsequent relative permeability calculations [20]. Brine viscosity was 0.50 cP at test conditions (30 MPa, 77 °C). scCO_2 and N_2 viscosities (0.068 and 0.027 cP) were taken from the literature. scCO_2 and nitrogen (N_2) were supplied from high-purity cylinders and brought to test conditions (30 MPa pore pressure, 77 °C) upstream of the core. Crucially, to prevent transient mass transfer, localized fluid evaporation, and salt precipitation during the coreflood, both the non-wetting phases and the brine were thoroughly pre-equilibrated at the exact test temperature and pressure prior to injection.

Table 1. Steady-state coreflood programme and absolute permeabilities. All three corefloods used the same Berea plug. The N_2 test and scCO_2 test #1 were run on the clean plug (k_w = 63.1 and 61.8 mD, respectively); an intermediate, unreported coreflood was then performed without re-cleaning the core, irreversibly reducing the permeability to k_w = 31.6 mD for scCO_2 test #2 (re-cleaning after test #2 did not restore it; see Section 4.4). PD = primary drainage; IMB = imbibition; 2nd DRN = secondary drainage.

Test ID	Non-wetting fluid	Cycles performed	Abs. gas perm. before [mD]	Abs. gas perm. after [mD]	Abs. brine perm. [mD]
N_2 test	N_2	PD → IMB → 2nd DRN	133	89.3	63.1
scCO_2 test #1	scCO_2	PD → IMB → 2nd DRN	131	88.4	61.8
Intermediate test	-	not reported; core not re-cleaned afterward	-		-
scCO_2 test #2	scCO_2	PD → IMB → 2nd DRN	57.6	44.5	31.6

2.3 Steady-State saturation and flow design

A single Berea core plug was used for all three corefloods, each run with the identical full-cycle schedule (primary drainage → imbibition → secondary drainage): the N_2-brine test and $scCO_2$-brine tests #1 and #2 (Table 1). The N_2 test and $scCO_2$ test #1 were conducted on the clean plug at an absolute brine permeability of ≈63.1 mD. An intermediate coreflood was then performed without subsequently re-cleaning the core, reducing the brine permeability to 31.6 mD for $scCO_2$ test #2; this reduction proved irreversible (Section 4.4).

The specific fractional flow schedule and injection parameters were carefully planned to optimize data resolution and satisfy theoretical flow assumptions. Because of the high mobility of the non-wetting gas phases, an evenly spaced fractional flow schedule naturally results in highly clustered saturation points. To achieve a near-equal saturation spacing across the relative permeability curve, the f_g schedule was non-linearly distributed. Smaller fractional increments were heavily concentrated near the displacement endpoints (e.g., f_g = 0.01, 0.05, 0.95, 0.99) to accurately capture the sharp curvature of the relative permeability functions prior to reaching the saturation endpoints.

Rather than maintaining a constant total volumetric flow rate (Q_t), the displacements were dynamically controlled to maintain a targeted, stable differential pressure (ΔP) across the core. Because the viscosity of $scCO_2$ is significantly lower than that of brine, maintaining a constant Q_t across all fractional flows would induce massive fluctuations in ΔP. By adjusting Q_t to keep ΔP constant and relatively low, we ensured that the pressure-sensitive properties of $scCO_2$ (density and viscosity) remained constant along the length of the sample. This strategy rigorously satisfies the incompressible flow assumption inherent to the multiphase extension of Darcy's law. Furthermore, maintaining strict constraints on the differential pressure limits pressure-induced fluid mass transfer and promotes highly stable fluid interfaces within the high-pressure separator, ensuring precise material balance and saturation quantification [31].

Steady state at each fractional flow was defined when the inlet/outlet pressures, the differential pressure across the core, and the separator fluid levels were stable. After reaching minimum water saturation ($S_{w,min}$) during 100% gas injection, the cycle was reversed to imbibition by incrementally increasing the brine fractional flow back to 1.0, and was subsequently followed by the secondary drainage cycle. Effluent production and stepwise interface-level changes were monitored continuously with the precision separator to infer average system saturations via material balance.

3 Results

3.1 Primary drainage

Steady-state relative permeability curves for both $scCO_2$-brine and N_2-brine systems in the clean Berea sandstone core are shown in **Fig. 3**. The primary drainage branches exhibit the characteristic multiphase flow behavior and hysteresis reported for quartzose sandstones at reservoir conditions [2,16]. For the $scCO_2$-brine system, the two corefloods reached minimum water saturations at maximum gas fractional flow ($S_{w,min}$) of 0.37 and 0.48, with maximum gas relative permeabilities ($k_{rg,max}$) of 0.69 and 0.31, respectively. The N_2-brine system produced comparable endpoints ($S_{w,min}$ = 0.47, $k_{rg,max}$ = 0.39). We use $S_{w,min}$ rather than "irreducible water saturation" because, without in-situ saturation monitoring and a measured capillary-pressure curve, the saturation reached at $f_g \rightarrow 1$ is the terminal value under the conditions applied rather than a true connate value (Section 4.4).

A)

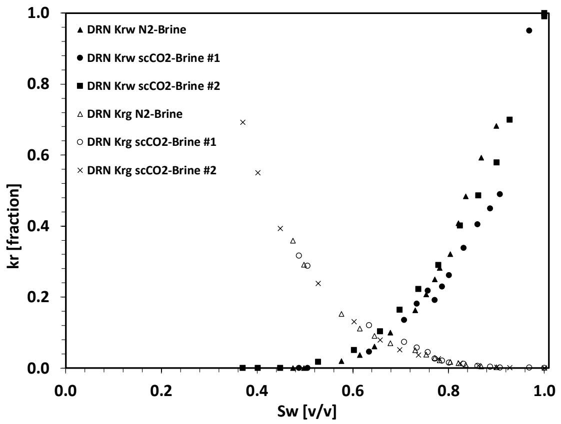

B)

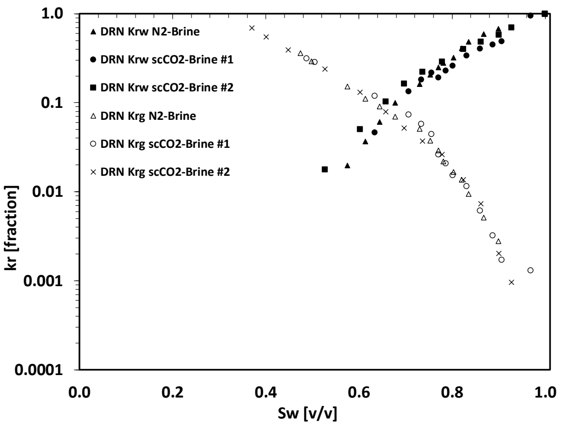

Fig. 3. Steady-state relative permeability for the $scCO_2$-brine and N_2-brine systems during primary drainage in the clean Berea sandstone core at reservoir conditions (30 MPa, 77 °C), shown on (a) linear and (b) semi-logarithmic scales. Each plot compares the two $scCO_2$ corefloods (tests #1 and #2) against the strongly water-wet N_2 surrogate baseline.

Applying a standard Corey parameterization to the experimental data yielded Corey exponents of n_w = 2.9 and n_g = 3.1 for the $scCO_2$-brine test #1, n_w = 2.8 and n_g = 2.9 for the $scCO_2$-brine test #2, and n_w = 2.2 and n_g = 2.9 for the N_2-brine system. These exponents align with the expected ranges for strongly water-wet sandstones, directly providing simulation-ready inputs for modeling plume mobility.

3.2 Imbibition and residual capillary trapping

Following primary drainage, the imbibition branches (**Fig. 4**) generated residual gas saturations (S_{gr}) of 0.37 for $scCO_2$ test #1 and 0.33 for test #2, and 0.35 for N_2. This translates to a trapping efficiency (the ratio of S_{gr} to the maximum initial gas saturation, S_{gi}) of approximately 59-64% for the $scCO_2$ system and 66% for the N_2 system. Importantly, this direct comparison confirms that there is no unusual hysteresis between primary drainage and imbibition for $scCO_2$ when compared to standard non-wetting gas surrogates like nitrogen, corroborating recent steady-state observations in the literature [21].

The experimental hysteresis data aligns well with the empirical Land trapping model [8], Land trapping coefficient of $C = 1$ (**Fig. 5**).

A)

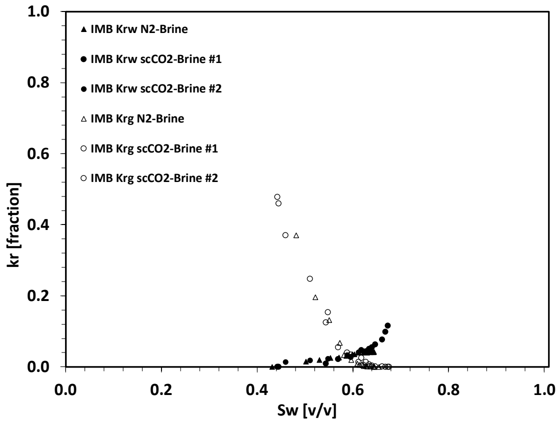

B)

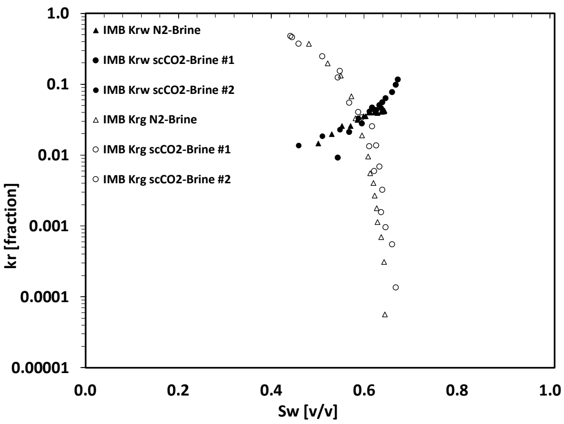

Fig. 4. Steady-state relative permeability during imbibition for the same systems and conditions, shown on (a) linear and (b) semi-logarithmic scales.

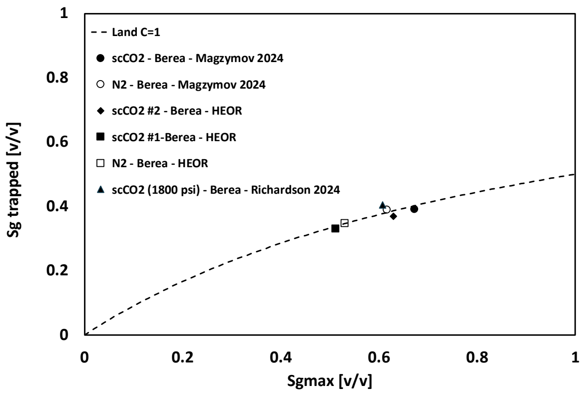

Fig. 5. Residual capillary trapping in the Berea sandstone core: residually trapped gas saturation (S_{gr}) at the end of imbibition versus the maximum initial gas saturation ($S_{gi,max}$) at the end of primary drainage. Data from this study ($scCO_2$ tests #1 and #2 and the N_2 test) are shown together with published steady-state residual-trapping data for Berea sandstone ([21], $scCO_2$ and N_2; [32], $scCO_2$). Datasets were included on the basis of rock type and measurement method (steady-state corefloods on Berea sandstone) and not on the basis of agreement with the present data. The broader set of residual-trapping benchmarks, spanning different rock states, fluids (e.g., $scCO_2$-water), methods, and pressure/temperature conditions, and a correspondingly wider range of trapping efficiencies, is compiled in Table 2. The solid curve is the empirical Land trapping model with a coefficient C = 1.

3.3 Secondary drainage and saturation cycling

During the secondary-drainage cycles the relative permeability curves retraced the primary-imbibition path (**Fig. 4** and **Fig. 6**). It is important to distinguish two forms of hysteresis here. The drainage-imbibition hysteresis, which governs residual capillary trapping and underpins storage security, is strong and is fully captured by the Land model (Section 3.2). What we additionally observe is that secondary drainage introduces no further, complex scanning loops relative to primary imbibition. This absence of additional secondary-cycle hysteresis is itself a useful result, because it simplifies the inputs required to model reinjection and fluctuating well pressures: a drainage-imbibition curve together with the Land trapping relation suffices [21].

A)

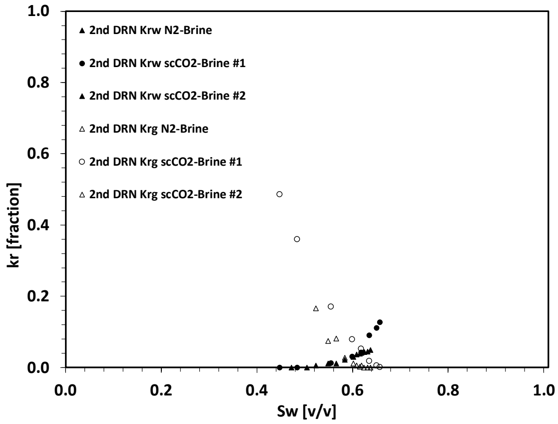

B)

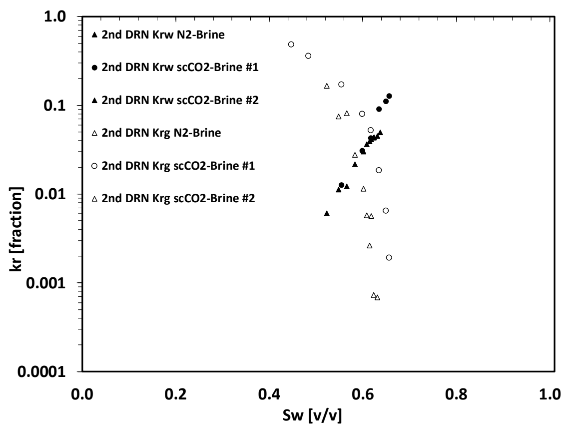

Fig. 6. Steady-state relative permeability during secondary drainage for the same systems and conditions, shown on (a) linear and (b) semi-logarithmic scales. The secondary-drainage curves retrace the primary-imbibition path (**Fig. 4**).

4 Discussion

The measured relative permeability curves and trapping characteristics (Section 3) are compared here with established empirical models and the wider literature.

4.1 Benchmarking against literature

Table 2 merges the former endpoint and trapping comparisons. It places the present endpoints, Corey exponents, maximum initial and residual gas saturations, and trapping efficiencies alongside highly cited Berea and clean-sandstone datasets, with the method used to establish the water-saturation endpoint in each study.

The measured endpoints are consistent with classical strongly water-wet benchmarks: as shown by [2,26], $scCO_2$-brine displacements in Berea are essentially indistinguishable from the analog N_2-water and oil-water data of [42], and the Corey exponents fall in the expected range for water-wet sandstones. The trapping efficiencies and the C = 1 fit fall within the bounds reported by [1,43].

4.2 Suitability of N_2 as a surrogate: interfacial tension, viscosity contrast, and wettability

The endpoints and curve shapes reported in Section 3 indicate that both fluid systems are strongly water-wet, in agreement with the capillary-pressure and contact-angle evidence for Berea in the presence of $scCO_2$ cited above [17,18]. In every test the brine and gas relative permeability curves cross at a high water saturation ($S_w \approx$ 0.65, 0.67, and 0.66 for $scCO_2$ tests #1 and #2 and the N_2 test; **Fig. 3**a), and a crossover above $S_w = 0.5$ is a standard indicator of water-wet behaviour. Consistently, the minimum water saturations are high ($S_{w,min} = 0.37$ to 0.48) and the brine relative permeability at the end of imbibition is low ($k_{rw} = 0.04$, 0.12, and 0.04 at S_{gr}; **Fig. 4**), well below the values expected for an intermediate- or non-water-wet rock.

The asymmetry of hysteresis between the two phases reinforces this interpretation. The brine relative permeability is essentially reversible, its drainage and imbibition branches nearly coinciding (**Fig. 3** and **Fig. 4**), whereas the gas relative permeability is strongly hysteretic, with the imbibition branch lying below the drainage branch and falling to zero while a substantial trapped gas saturation remains ($S_{gr} \approx 0.33$ to 0.37). A reversible wetting phase combined with a hysteretic, trappable non-wetting phase is characteristic of strongly water-wet media. Because in-situ saturation monitoring, a measured capillary-pressure curve, and a direct contact-angle measurement were outside the scope of this work, these are inferences from the shape and endpoints of the relative permeability curves rather than a direct wettability measurement; they are nonetheless mutually consistent and agree with the independent Berea/$scCO_2$ data cited above. Notably, the $scCO_2$-brine system reproduces the same water-wet signatures as the N_2-brine system, indicating that $scCO_2$ did not shift the wetting state of the clean Berea toward intermediate-wet under the present conditions.

Although N_2 and $scCO_2$ reproduce nearly identical relative permeability curves in this clean, water-wet sandstone, the two fluids differ in properties that can in principle affect multiphase flow: $scCO_2$ has a higher density and viscosity than N_2 and a lower interfacial tension (IFT) with brine, and its phase behaviour is more sensitive to pressure and temperature. With the present fluid properties (brine 0.50 cP, $scCO_2$ 0.068 cP, N_2 0.027 cP) the non-wetting/wetting viscosity ratio is $M \approx 0.14$ for $scCO_2$-brine and $M \approx 0.054$ for N_2-brine, while the brine IFT is ≈ 30-35 mN/m for $scCO_2$ versus ≈ 60-70 mN/m for N_2 [18]. **Fig. 7** plots these viscosity contrasts against IFT for the two systems. That the intrinsic curves nonetheless coincide is consistent with the viscous-limit argument of Reynolds and Krevor [16]. Once capillary-heterogeneity effects are suppressed by sufficiently high flow rates, the differences in IFT and viscosity contrast do not translate into measurable differences in intrinsic relative permeability. This supports the use of N_2 as a surrogate for clean, strongly water-wet sandstones.

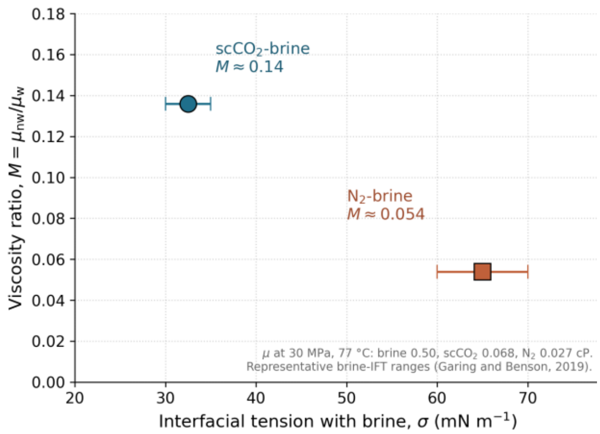

Fig. 7. Non-wetting/wetting viscosity ratio M versus brine interfacial tension for the $scCO_2$-brine and N_2-brine systems at 30 MPa and 77 °C. Viscosities: brine 0.50 cP, $scCO_2$ 0.068 cP, N_2 0.027 cP. Representative brine-IFT ranges from [18].

4.3 Interpretation of hysteresis

Two forms of hysteresis must be distinguished. The drainage-imbibition hysteresis, which governs residual capillary trapping and underpins storage security, is strong and is fully captured by the Land model (C = 1). What the secondary-drainage cycle adds is minimal: it retraces the primary-imbibition path with no complex secondary scanning loops. This absence of additional secondary-cycle hysteresis simplifies the inputs required to model reinjection and fluctuating well pressures, since a single drainage curve together with the Land relation suffices.

Table 2. Relative permeability endpoints, Corey exponents, and residual capillary trapping characteristics for the present tests and selected Berea / legacy sandstone benchmarks (former Tables 2 and 3 combined). $S_{w,min}$ is the water saturation at the maximum gas fractional flow ($f_g \rightarrow 1$); for the present tests this is a flow endpoint under the imposed conditions rather than a true irreducible saturation (Section 4.4; see the method column). S_{gr}/S_{gi} is the trapping efficiency. ISSM = in-situ saturation monitoring.

Reference	Fluid system	Conditions	$S_{w,min}$	$k_{rg,max}$	Corey n_w/n_g	$S_{gi,max}$	S_{gr}	S_{gr}/S_{gi}	S_w-endpoint method
This Study-scCO2 test #1	$scCO_2$ - Brine	30 MPa, 77 °C	0.37	0.69	2.9 / 3.1	0.63	0.37	59%	Steady-state, endpoint at f_g = 1 (no ISSM)
This Study $scCO_2$ test #2	$scCO_2$ - Brine	30 MPa, 77 °C	0.48	0.31	2.8 / 2.9	0.51	0.33	64%	Steady-state, endpoint at f_g = 1 (no ISSM)
This Study N_2 test #1	N_2 - Brine	30 MPa, 77 °C	0.47	0.39	2.2 / 2.9	0.53	0.35	66%	Steady-state, endpoint at f_g = 1 (no ISSM)
Richardson et al. (2025)	$scCO_2$ - Brine	30 MPa, 77 °C	0.40	0.79	N/A	0.60	0.40	67%	Steady-state (recirculation)
Magzymov et al. (2024)	N_2 - Brine	30 MPa, 77 °C	0.38	0.56	N/A	0.62	0.39	63%	Steady-state (recirculation)
Chen et al. (2016)	$scCO_2$ - Brine	10.3 MPa, 20 °C	0.20 - 0.40	0.40 - 0.80	N/A	N/A	N/A	N/A	Steady-state (fractional flow)
Krevor et al. (2012)	$scCO_2$ - Water	9 MPa, 50 °C	0.20	> 0.50	N/A	>0.80	0.31	~38%	Steady-state, X-ray CT (ISSM)
Oak et al. (1990)	N_2 - Water	Ambient	0.22 - 0.28	0.60 - 0.80	N/A	N/A	N/A	N/A	Steady-state
Perrin & Benson (2010)	$scCO_2$ - Brine	12.4 MPa, 50 °C	0.62	0.06	N/A	N/A	N/A	N/A	Steady-state, X-ray CT (ISSM)
Burnside & Naylor (2014)	$scCO_2$-brine	N/A	N/A	N/A	N/A	0.31	0.21	67%	Compiled/review
Pentland et al. (2011)	$scCO_2$-brine	9.0 MPa, 70 °C	N/A	N/A	N/A	0.85	0.35	41%	porous-plate coreflood, mass balance
Akbarabadi & Piri (2013)	$scCO_2$-brine	11.0 MPa, 55 °C	N/A	N/A	N/A	0.55-0.65	0.20-0.31	49%-61%	Steady-state, micro-CT (ISSM)
Zuo & Benson (2014)	$scCO_2$-water	12.41 MPa, 50 °C	0.80	N/A	N/A	0.20	0.10	50%	X-ray CT (ISSM)

4.4 Limitations and future work

The absolute permeability of the single core plug decreased from 61.8 mD ($scCO_2$ test #1) to 31.6 mD ($scCO_2$ test #2). This reduction followed an intermediate coreflood that was performed without subsequently re-cleaning the core, and it proved permanent: re-cleaning the plug with toluene and methanol after test #2 did not restore the original permeability. The irreversibility indicates a change to the pore structure, most consistent with mechanical mobilisation and re-bridging of kaolinite/quartz fines, rather than transient blockage by residual fluids, and is unlikely to be related to chemical reactions with $scCO_2$, as no significant chemical alteration of the rock was observed. Because each relative-permeability value is normalised by the absolute permeability of the core in its corresponding state, the reported k_r curves are unaffected.

The reported relative permeabilities carry uncertainty from the pressure-transducer accuracy (±0.01 % full scale), the material-balance determination of saturation, and the absence of in-situ saturation monitoring. The tabulated values (Appendix A) should be read with this uncertainty in mind.

The present study did not employ in-situ saturation monitoring (ISSM), and the intercept method was not applied to all steady-state fractional flow steps. These limitations introduce minor additional uncertainty in saturation determination and the calculation of relative permeability endpoints. Where ISSM or comprehensive intercept methods are unavailable, alternative approaches such as multi-rate bump checks or numerical pressure-history matching must be utilized to mathematically diagnose and correct for capillary end effects [14,43,46,47]. Future work will incorporate ISSM (e.g., X-ray CT or gamma-ray attenuation) and apply the intercept method consistently across all fractional flows to further isolate and reduce experimental boundary artefacts. Additionally, future experimental workflows should couple these relative permeability tests with full-cycle drainage and imbibition capillary pressure measurements utilizing the semi-dynamic method [48,49] to develop a consistent set of inputs for reservoir simulation. Furthermore, while the current study establishes robust baselines at a single thermodynamic state representative of deep saline formations (30 MPa and 77 °C), CO_2 multiphase flow behavior and mutual solubility are highly sensitive to phase changes. Future evaluations must incorporate sensitivity analyses across different pressure conditions to assess how reservoir depletion or repressurisation alters relative permeability endpoints and hysteresis behavior, building upon recent high-pressure investigations in sandstones [31,42].

5 Conclusions

This study has presented a systematic steady-state relative permeability investigation of $scCO_2$-brine and N_2-brine systems in a benchmark homogeneous Berea sandstone under identical high-pressure, high-temperature reservoir conditions (30 MPa, 77 °C). By applying the same rigorous fractional-flow schedule and continuous phase-equilibration to both fluid pairs, a direct, artifact-free quantitative comparison was achieved across full saturation paths, uniquely encompassing primary drainage, imbibition, and the rarely reported secondary drainage cycle.

Key findings confirm that nitrogen can serve as surrogate for $scCO_2$ in laboratory relative permeability measurements within chemically inert, water-wet porous media. The N_2-brine curves closely reproduced the $scCO_2$-brine curves, yielding nearly identical minimum water saturations, maximum gas relative permeabilities, and Land trapping coefficients. Crucially, these measurements are consistent with classical, strongly water-wet benchmark data and established empirical hysteresis models for clean quartzose sandstones, confirming that $scCO_2$ does not exhibit unusually low endpoint permeabilities when capillary end effects are mitigated [2,38].

Drainage-imbibition hysteresis and the resulting residual trapping are strong and well represented by the Land model, whereas the secondary-drainage cycle introduces no additional complex scanning loops, simplifying the inputs required to model reinjection and fluctuating well pressures.

While establishing these high-confidence baselines on a standard outcrop sample is a critical first step to isolating fluid-specific physics from geochemical reactions, translating these findings to actual field developments requires further validation. Future studies must apply these steady-state protocols to complex heterogeneous lithologies and legacy cores from depleted oil and gas fields, which often exhibit altered wettability and complex structural degradation not present in pristine outcrops.

Ultimately, this comprehensive, literature-validated dataset reinforces the validity of using N_2 as a non-wetting analog and deploying standard Corey-type and Land parameterizations for homogeneous sandstones. By filling the critical gap in full-cycle saturation data, these findings will improve the accuracy of reservoir simulations for plume migration, injectivity, and long-term residual capillary trapping, thereby supporting the safe and efficient deployment of geological carbon storage at scale.

Acknowledgments

This project is supported by the Hebron and Hibernia Projects and is managed by Energy Research & Innovation Newfoundland & Labrador (ERI). Any opinions, findings, and conclusions or recommendations expressed in this publication are those of the author(s) and do not necessarily reflect the views of the Hebron Project, Hibernia Project, ExxonMobil or ERI.

References

1. N.M. Burnside, M. Naylor, Int. J. Greenh. Gas Control **23**, 1-11 (2014)
2. S.C.M. Krevor, R. Pini, L. Zuo, S.M. Benson, Water Resour. Res. **48**, W02532 (2012)
3. S.C.M. Krevor, R. Pini, B. Li, S.M. Benson, Geophys. Res. Lett. **38,** L15401 (2011)
4. T. Acharya, T. Dhaliwal, A. Ludian, G. Popli, B. Wilemon, L. Hernandez, M. Farahani, L. Song, Processes **12**, 2176 (2024)
5. L. Zuo, S.M. Benson, Geophys. Res. Lett. **41**, 2820-6 (2014)
6. C. Ruprecht, R. Pini, R. Falta, S. Benson, L. Murdoch, Int. J. Greenh. Gas Control **27**, 15-27 (2014)
7. C. Reynolds, M. Blunt, S. Krevor, Energy Procedia **63**, 5577-85 (2014)
8. C.S. Land, Soc. Pet. Eng. J. **8**, 149-56 (1968)

9. M. Flett, R. Gurton, I. Taggart, SPE 88485-MS (2004)
10. R. Juanes, E.J. Spiteri, F.M. Orr Jr., M.J. Blunt, Water Resour. Res. **42,** W12418 (2006)
11. E.J. Spiteri, R. Juanes, M.J. Blunt, F.M. Orr, SPE J. **13**, 277-88 (2008)
12. C. Doughty, Energy Convers. Manag. **48**, 1768-81 (2007)
13. L.S. Lun, B. Gao, P. Krishnamurthy, K. Kohli, R.C. Wattenbarger, SPE, D031S113R002 (2023)
14. M. Mascle, A. Oisel, P.K. Munkerud, E. Ebeltoft, O. Lopez, C. Pryme, S. Youssef, Petrophysics **66**, 26-43 (2025)
15. N. Müller, Transp. Porous Media **87**, 367-83 (2011)
16. C.A. Reynolds, S. Krevor, Water Resour. Res. **51**, 9464-89 (2015)
17. A. Al-Menhali, B. Niu, S. Krevor, Water Resour. Res. **51**, 7895-914 (2015)
18. C. Garing, S.M. Benson, Geophys. Res. Lett. **46**, 776-82 (2019)
19. A. Laesecke, C.D. Muzny, J. Phys. Chem. Ref. Data **46**, 013107 (2017)
20. A. Haghi, R. Chalaturnyk, Int. J. Greenh. Gas Control **135**, 104159 (2024)
21. D. Magzymov, G. Jerauld, E. Lyons, S. Richardson, L. Lun, SPE 221051-MS (2024)
22. J. Schembre-McCabe, M. Akbarabadi, J. Burger, M. Rauschhuber, W. Richardson, Petrophysics **66**, 969-81 (2025)
23. X. Chen, S. Gao, A. Kianinejad, D.A. DiCarlo, Water Resour. Res. **53**, 6312-21 (2017)
24. M. Faramarzi, S.M. Tabatabaei, B. Sedaee, N. Attari, S.A. Panahi, Capillarity **14**, 35-52 (2025)
25. B. Gao, L. Lun, R.C. Wattenbarger, SSRN (2024)
26. R. Pini, S.C.M. Krevor, S.M. Benson, Adv. Water Resour. **38**, 48-59 (2012)
27. L. Tang, G. Ding, S. Song, H. Wang, W. Xie, Y. Zhou, Z. Song, C. Xie, H. Song, Water **15**, 4235 (2023)
28. D.B. Bennion, S. Bachu, SPE Reserv. Eval. Eng. **11**, 487-96 (2008)
29. T.D. Rathnaweera, P.G. Ranjith, M.S.A. Perera, K.M.A.S. Bandara, W.A.M. Wanniarachchi, A.S. Ranathunga, J. Nat. Gas Sci. Eng. **45**, 609-24 (2017)
30. T. Akın, S. Erol, A.B. Tokel, D.B. Sevindik, S. Akın, Int. J. Greenh. Gas Control **146**, 104413 (2025)
31. H. Ott, K. de Kloe, F. Marcelis, A. Makurat, Energy Procedia **4**, 4425-32 (2011)
32. S. Richardson, B. Gao, E. Lyons, D. Magzymov, L. Poore, G. Besil, L. Lun, Petrophysics **66**, 44-53 (2025)
33. L. Griffiths, J. Dautriat, J. Park, I. Vera Rodriguez, K. Iranpour, G. Sauvin, J. Sarout, L. Grande, V. Oye, M. Soldal, D.N. Dewhurst, N.H. Mondol, J.C. Choi, SSRN (2021)
34. A. Busch, P. Bertier, Y. Gensterblum, G. Rother, C.J. Spiers, M. Zhang, H.M. Wentinck, Geomech. Geophys. Geo-Energy Geo-Resour. **2**, 111-30 (2016)
35. K. War, G. Raveendran, D.N. Arnepalli, Int. J. Greenh. Gas Control **119**, 103696 (2022)
36. F. Othman, M. Yu, F. Kamali, F. Hussain, J. Nat. Gas Sci. Eng. **56**, 344-57 (2018)
37. J. Ge, X. Zhang, F. Othman, Y. Wang, H. Roshan, F. Le-Hussain, Int. J. Greenh. Gas Control **103**, 103184 (2020)
38. T. Zhang, T. Ming, L. Yuan, G. Zhu, C. Zhang, Y. Liu, L. Yanfang, W. Wen, Y. Xin, Energy **278**, 127874 (2023)
39. X. Chen, Doctoral dissertation, The University of Texas at Austin (2016)
40. X. Chen, A. Kianinejad, D.A. DiCarlo, Water Resour. Res. **52**, 8374-83 (2016)
41. J. Moore, P. Holcomb, D. Crandall, S. King, J.-H. Choi, S. Brown, S. Workman, Adv. Water Resour. **153**, 103953 (2021)
42. M.J. Oak, L.E. Baker, D.C. Thomas, J. Pet. Technol. **42**, 1054-61 (1990)
43. M. Akbarabadi, M. Piri, Adv. Water Resour. **52**, 190-206 (2013)
44. J.-C. Perrin, S.M. Benson, Transp. Porous Media **82**, 93-109 (2010)
45. C.H. Pentland, R. El-Maghraby, S. Iglauer, M.J. Blunt, Geophys. Res. Lett. **38**, L06401 (2011)
46. R. Farokhpoor, B.J.A. Bjørkvik, E. Lindeberg, O. Torsæter, Energy Procedia **37**, 5339-51 (2013)
47. R. Gupta, D.R. Maloney, SPE Reserv. Eval. Eng. **19**, 316-30 (2016)
48. J. Ge, X. Zhang, F. Le-Hussain, Energy **239**, 122233 (2022)
49. D. Magzymov, G. Jerauld, L. Lun, J. Golias, K. Vidal, A. Foernes, T. Danielsen, SPE 227909-MS (2025)

Appendix A

Table 3. Primary drainage, primary imbibition, and secondary drainage steady-state relative permeability for $scCO_2$-brine and N_2-brine at 77 °C (170 °F), 30 MPa (4350 psi), 4 wt% NaCl.

f_w	q_t [cc/min]	ΔP [psi]	S_w [v/v]	k_{rg}	k_{rw}
				[frac K_w (S_w=1)]	
Primary drainage ($scCO_2$) - test #1					
1	0.5	18.46	1.00	0.00	1.00
0.99	1	27.44	0.92	0.00	0.70
0.975	1	30.1	0.90	0.01	0.58
0.9	1	31.76	0.86	0.01	0.49
0.8	1	33.14	0.82	0.01	0.40
0.6	1	33.93	0.78	0.03	0.29
0.45	1	33.46	0.74	0.04	0.2
0.3	1	31.58	0.70	0.05	0.16
0.15	1	27.84	0.66	0.08	0.10
0.05	1.5	28.11	0.60	0.13	0.05
0.01	1.5	21.85	0.53	0.24	0.02
0	1.5	18.6	0.45	0.39	0.00
0	3	20.8	0.40	0.55	0.00
0	6	25.12	0.37	0.69	0.00
Primary imbibition ($scCO_2$) - test #1					
0	0.5	14.3	0.37	0.81	0.00
0	1.5	15.8	0.36	0.80	0.00
0.005	1.5	18.9	0.46	0.37	0.01
0.01	1.5	21.54	0.51	0.25	0.02
0.02	1.5	26.4	0.55	0.15	0.02
0.1	1	43.5	0.59	0.04	0.03
0.3	0.8	70.9	0.61	0.01	0.04
0.5	0.4	59	0.62	0.01	0.04
0.8	0.3	65.3	0.63	0.01	0.05
1	0.2	65	0.63	0.00	0.04
Secondary drainage ($scCO_2$) - test #1					
1	0.2	54.9	0.60	0.00	0.05
1	0.1	33.9	0.62	0.00	0.05
1	0.05	23.4	0.64	0.00	0.05
0.9	0.1	33.1	0.63	0.00	0.04
0.5	0.1	25.32	0.62	0.01	0.04
0.02	0.2	16.7	0.57	0.08	0.01
0.005	0.4	16.7	0.52	0.17	0.01
0	0.5	16.4	0.52	0.23	0.00
Primary drainage ($scCO_2$) - test #2					
1	1	19.361	1.00	0.00	1.00
0.99	1.5	21.36	0.97	0.00	0.95
0.975	1.5	28.56	0.91	0.00	0.49
0.95	1.5	29.46	0.89	0.00	0.45
0.9	1.5	30.32	0.86	0.01	0.40
0.8	2	37.31	0.83	0.01	0.34
0.7	2	40.52	0.80	0.01	0.26
0.6	2	39.89	0.79	0.02	0.23
0.5	2	39.77	0.77	0.03	0.19
0.4	2.5	36.64	0.76	0.04	0.22
0.3	2.5	34.3	0.73	0.06	0.18
0.2	2.5	32.19	0.71	0.07	0.13
0.05	3	29.81	0.63	0.12	0.05
0	4	23.03	0.50	0.29	0.00
0	8	30.88	0.49	0.32	0.00
Primary imbibition ($scCO_2$) - test #2					
0	8	25.43	0.44	0.46	0.00
0	4	19.23	0.44	0.48	0.00
0.01	4	35.4	0.54	0.12	0.01
0.05	3	49.29	0.57	0.05	0.02
0.1	2	50.02	0.60	0.03	0.03
0.2	2	57.01	0.62	0.02	0.04
0.3	1.5	66.44	0.63	0.01	0.04
0.5	1	63.80	0.63	0.01	0.05
0.7	0.5	45.55	0.64	0.00	0.06
0.9	0.4	42.34	0.65	0.00	0.06
0.95	0.3	32.275	0.66	0.00	0.08
0.99	0.3	28.75	0.67	0.00	0.10
1	0.3	26.6	0.67	0.00	0.12
1	0.6	37.63	0.68	0.00	0.12
Secondary drainage ($scCO_2$) - test #2					
0.9	0.5	31.3	0.64	0.00	0.13
0.7	0.5	29.3	0.63	0.00	0.11
0.4	0.7	29.06	0.62	0.02	0.09
0.1	1	25.21	0.60	0.05	0.04
0.05	1.5	25.72	0.58	0.08	0.03
0.01	3	25.39	0.54	0.17	0.01
0	4	21.1	0.47	0.36	0.00
0	8	24.77	0.43	0.49	0.00
Primary drainage (N_2)					
1	2	20.93	1.00	0.00	1.00
1	4	28.61	1.00	0.00	1.00
0.99	1.5	20.40	0.95	0.00	0.81
0.975	2	23.23	0.93	0.00	0.75
0.95	2	23.97	0.90	0.00	0.68
0.9	2	24.91	0.87	0.01	0.59
0.8	2	25.93	0.84	0.01	0.48
0.7	2	26.39	0.82	0.01	0.41
0.6	2	27.54	0.80	0.02	0.32
0.5	2	26.85	0.78	0.02	0.28
0.4	2.5	28.56	0.77	0.03	0.25
0.3	2.5	27.08	0.75	0.04	0.21
0.2	2.5	25.03	0.73	0.05	0.16
0.1	3	24.82	0.68	0.07	0.10
0.05	3	22.71	0.64	0.09	0.06
0.025	3	21.17	0.61	0.11	0.04
0.01	3	19.20	0.58	0.15	0.02
0	4	17.50	0.50	0.29	0.00
0	8	20.01	0.47	0.36	0.00
0	12	22.50	0.47	0.39	0.00
Primary imbibition (N_2)					
0	12	21.70	0.48	0.37	0.00
0.005	8	23.80	0.52	0.20	0.01
0.01	6	24.90	0.55	0.13	0.02
0.025	3	24.50	0.57	0.07	0.03
0.05	2	28.10	0.58	0.03	0.03
0.1	1.5	31.60	0.60	0.02	0.03
0.2	0.75	29.40	0.61	0.01	0.04
0.3	0.4	26.30	0.61	0.01	0.04
0.4	0.4	28.60	0.62	0.00	0.04
0.5	0.3	27.70	0.62	0.00	0.04
0.6	0.2	24.90	0.63	0.00	0.04
0.7	0.15	23.50	0.63	0.00	0.04
0.8	0.15	24.50	0.64	0.00	0.04
0.9	0.15	25.80	0.64	0.00	0.04
0.98	0.1	22.50	0.64	0.00	0.04
1	0.1	22.30	0.65	0.00	0.04
Secondary drainage (N_2)					
1	0.1	22.08	0.62	0.00	0.04
0.8	0.3	34.20	0.62	0.00	0.04
0.5	0.3	27.80	0.62	0.00	0.04
0.3	0.4	25.80	0.61	0.01	0.04
0.15	0.5	22.78	0.60	0.01	0.03
0.05	1	22.12	0.58	0.03	0.02
0.01	2	20.16	0.55	0.08	0.01
0	4	18.97	0.50	0.18	0.00
0	8	20.71	0.47	0.28	0.00